NMR Imaging in porous media

Sharapov B. Andrey

24th May 2006

Abstract

In the first part I consider basics of NMR and NMR Imaging. We introduce such notions as magnetization, phase and frequency encoding techniques as well as examples of its application. In the second part only application of imaging is considered, given a lot of details and pictures.

Contents

Part I
Theory of NMR and NMR Imaging.

1 The very basics of NMR.

If one dissects the abbreviation NMRI into its individual words, the essential features of the method are all covered: we are exploiting the interaction of the Nuclear magnetic properties with external static Magnetic fields that leads to Resonance phenomena with oscillating magnetic fields in the radiofrequency regime in order to obtain an Image of an object. The use of the term "nuclear" has become so unpopular in medical sciences that the abbreviation "MRI" is more common nowadays; although the "N" just states that the experiment is performed on the atomic nuclei, which make up all matter, including our body - to distinguish it from techniques that use the response of the electron. We should merely keep in mind that we are dealing with a quantum mechanical phenomenon. However, most of the systems that are relevant to NMR imaging are weakly coupled homonuclear systems of solution or soft materials where motional averaging and secular approximations are valid for simplified classical description to be sufficient. If one wants to exploit, e.g., the dipolar coupled spin network in ordered soft materials or large molecular assemblies for contrast imaging, a more detailed knowledge of the quantum mechanical relationships becomes inevitable. We attempt to describe NMR Imaging in a simplified manner using only three essential equations that explain why we see a signal and what it looks like. The first equation describes the nuclear spin magnetization, thus the strength of the NMR signal (and indeed much more):

$$\mathbf{M}_0 = N\frac{\gamma^2\hbar^2 l(l+1)}{3k_B T}\mathbf{B}_0 \tag{1}$$

This equation is called the Curie law and relates the equilibrium magnetization $\mathbf{M}_0$ to the strength of the magnetic field $\mathbf{M}_0$. The constants have the following meaning: I is the nuclear spin quantum number (see below), γ is the gyromagnetic ratio specific for a given isotope, $\hbar$ is Planck's constant, k_B is Boltzmann's constant, N is the number of nuclei and T is the temperature. What it essentially tells us is that the magnetization increases linearly with the number of nuclei and the magnetic field, and with the square of the gyromagnetic ratio γ. $\mathbf{M}_0$ is the quantity which after all translates into the NMR signal that we measure, so it should be as large as possible. In order to obtain maximum magnetization, one therefore wants to use a very strong magnetic field, and take advantage of a nucleus with a large γ. Of all stable isotopes, the nucleus of the hydrogen atom, ^1H, has the largest γ. Furthermore, it is contained in all organic matter and the ^1H isotope has almost 100% natural abundance, which is the reason why the vast majority of imaging experiments are done with ^1H nuclei. The origin of the Curie law is found in the nuclear equivalent of the magnetization, the spin. It resembles a compass needle that is located at the core of the nucleus; brought into a magnetic field, its energy state will depend on its orientation relative to the field direction. The spin is a quantum property, i.e., it can only assume quantized (half-integer or integer) values, given by the total spin quantum number: $I = 0, +1/2, +1, ...$ The main difference from a real compass needle is that when a spin is brought into the magnetic field, all the different orientations it can assume correspond to only a limited number of discrete energy levels, quantized between I and $+I$ in half-integer steps, so that $2I+1$ possibilities result. One often symbolizes this effect by an arrow of a constant length that is oriented at well defined angles relative to $\mathbf{B}_0$, but this is merely a crutch for visualizing the quantum mechanical property through a classical one. Independent of how one imagines the spin, one needs to keep in mind that only by bringing the spins into an external magnetic field can the different orientations of the spins differ in energy, which - as stated above - takes place in a non-continuous but quantized fashion, with

energy differences of $E = \hbar\omega_0$, where ω_0 is the Larmor frequency. Its meaning will be discussed shortly. Keep in mind that not one but an ensemble of spins are present, which are distributed between the discrete energy levels. According to thermodynamics, the lower energy states are more likely to be populated - the average number of spins found in the different energy level states is given by the Boltzmann distribution:

$$\frac{n_{-\frac{1}{2}}}{n_{+\frac{1}{2}}} = exp\left(-\frac{\hbar\omega_0}{k_B T}\right) \tag{2}$$

Here we have restricted ourselves to the case of two energy levels as are found for $I = 1/2 : 1/2, +1/2$ (Figure 1). It describes the ^1H nucleus and many other isotopes that are important for imaging. The Curie law originates from the Boltzmann distribution. If we insert typical values for the magnetic field strength (say, 10 tesla) and room temperature (T = 298 K), we end up with a tiny fraction of 0.007% in population difference for the ^1H nuclei. This difference is what provides the NMR signal. If we add up all (quantum mechanical) spins to a (classical) bulk magnetization, most of them cancel out, but only this very small population difference determines the actual value of $\mathbf{M}_0$. For this reason NMR is traditionally regarded as an insensitive method. Although advanced techniques have made sample volumes down to nanolitres and concentrations down to micromolar detectable under certain circumstances, NMR spectroscopy and imaging can still not compete in terms of sensitivity with techniques such as fluorescence spectroscopy or atomic force microscopy, which are basically capable of detecting single atoms or molecules. However, the power of NMR lies in its unique ability to encode a cornucopia of parameters, such as chemical structure, molecular structure, alignment and other physical properties, interaction between atoms and molecules, incoherent dynamics (fluctuation, rotation, diffusion) and coherent flow (translation) of the sample into the complex

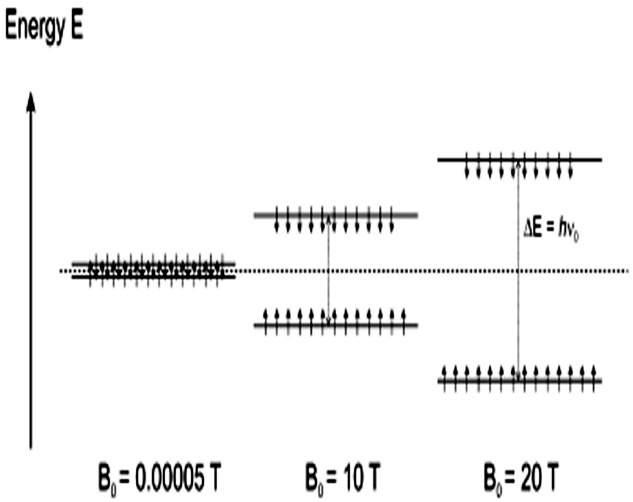

Figure 1: Schematic representation of the population difference of spins at different magnetic field strengths. The two different spin quantum number values of the ^1H spin, +1/2 and -1/2, are indicated by arrows. Spins assume the lower energy state preferentially, the ratio between "upper" and "lower" energy level being given by the Boltzmann distribution. The field strengths resemble typical values commonly used for high-resolution spectroscopy. The energy difference between the two states corresponds to the Larmor frequency, which is about 425 and 850 MHz for ^1H nuclei, respectively, at the two given fields of 10 and 20 T, respectively. For comparison, if the experiment had to be performed in the Earth's magnetic field (left part), the frequency would be as low as 2 kHz, which is in the audible range.

NMR signal, instead of simply measuring signal amplitudes of carriers that can be referred to distance or position information. The longitudinal magnetization $\mathbf{M}_0$, which we have just defined, is an equilibrium state for which a direct measurement would be of limited use for our purposes. The principle of NMR techniques, however, is not to measure this equilibrium quantity, but the response, thus the change of non-equilibrium transverse magnetization with time, which induces a voltage in a receiver coil enclosing the sample. When subjecting the spin system to an oscillating radiofrequency (rf) field, resonance phenomena can be utilized in such a way that, at the end of the irradiation, the magnetization $\mathbf{M}$ is manipulated to be oriented perpendicular to the magnetic field $\mathbf{B}_0$, i.e., out of its equilibrium. In this state, the spin ensemble's net magnetization is precessing about $\mathbf{B}_0$, and this precession takes place in a coherent manner ("in phase") among the spins in the ensemble as long as this coherence is not destroyed by natural or artificial influences. It turns out that controlling the time evolution of the coherence by means of a series of rf field and static magnetic field gradient pulses (pulse sequence) leaves a wealth of possibilities to encode information into the signal and extract it again at the time of acquisition. The time-dependence of $\mathbf{M}$ in the magnetic field, describing this precession motion, follows the second essential equation:

$$\frac{d\mathbf{M}}{dt} = \gamma \mathbf{M} \times \mathbf{B} \tag{3}$$

The time dependence of the magnetization vector,$\mathbf{M}(t)$, is thus related to the crossproduct of $\mathbf{M}$ and $\mathbf{B}$. Keep in mind also that the magnetic field can be timedependent. We have replaced $\mathbf{B}_0$ by $\mathbf{B}$ to indicate that the magnetic field can consist of different contributions. In particular, the rf field that interacts with the spins in the sample is a time-dependent magnetic field, $\mathbf{B}_{rf}$, it is precisely this field that, when taken into account during the application of the rf pulse, results in the magnetization being rotated out of its equilibrium orientation. To a first approximation, however, we consider the magnetic field to be static. We can then solve Eq. (3) and obtain:

$$\begin{aligned} M_x &= M_0 \sin \omega_0 t \\ M_y &= M_0 \cos \omega_0 t \\ M_+ &= M_0 \exp(i\omega_0 t) \end{aligned} \tag{4}$$

The quantity of interest is the precession of the components perpendicular to $\mathbf{B}_0$ that are measured in the experiment by induced voltage in the coil, which is subsequently amplified and demodulated. We can write them either as individual components M_x, M_y, or by a vector $\mathbf{M}_+$, which combines both of them. In the static field, the precession about B_0 occurs with the Larmor frequency ω_0=$\gamma\mathbf{B}_0$. If we neglect those processes which dampen the amplitude of the rotating transverse magnetization as precession proceeds, this already describes the frequency that we pick up with our receiver coil, and it is the third and perhaps the most important of our three fundamental equations of NMR:

$$\omega = \gamma |B| \tag{5}$$

Now what do we learn from this? Given that the gyromagnetic ratio γ is known for all nuclei with a very high precision, the measurement of the signal frequency ω_0 allows us to determine the actual value of the magnetic field precisely! Indeed this is what NMR is basically doing, with one remarkable exception: $\mathbf{B}$ is not just the externally applied field, but it is the magnetic field at the local position of the nucleus itself, which may vary from one nucleus to the other. A large part of the toolbox of NMR is built around this simple dependence. There are two regimes that can be distinguished, providing totally different information about our system. The microscopic regime is given by the immediate vicinity of the nucleus. It is surrounded by electrons the motion of which - just like the motion of any electric charge - induces a magnetic field that shields the nucleus from the external field, resulting in the nucleus specific

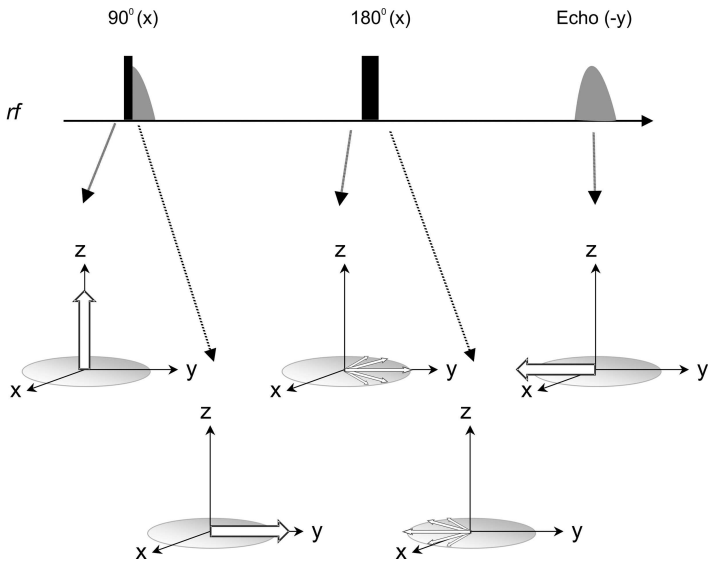

Figure 2: Behavior of the magnetization in a simple echo experiment. Top: a free induction decay (FID) follows the first 90° pulse; "x" denotes the phase of the pulse, i.e., the axis about which the magnetization is effectively rotated. The 180° pulse is applied with the same phase; the echo appears at twice the separation between the two pulses and its phase is inverted to that of the initial FID. Bottom: the magnetization vector at five stages of the sequence drawn in a coordinate frame rotating at ω_0 about the z axis. Before the 90° pulse, the magnetization is in equilibrium, i.e., parallel to the magnetic field (z); immediately after the 90° pulse, it has been rotated (by 90°!) into the transverse (x,y) plane; as it is composed of contributions from different parts of the sample, the slightly different local fields lead to a loss of coherence, i.e., to a free induction decay in the pick-up coil; before the 180° pulse, the different contributions (narrower arrows) have lost part or all of their coherence; after the 180° pulse, each partial magnetization has been flipped (by 180° !) due to the effect of the electromagnetic field of the pulse, but still sees the same, slightly different local fields; at a time corresponding to twice the pulse spacing, the different phase shifts relative to the average value have been reverted, all partial magnetizations are in phase again, and their signal contributions add up coherently - so a spin echo is generated.

local magnetic field. The single electron of the hydrogen atom shields a fraction of some 10^5 of the external field. Because the shielding depends on the actual charge distribution which, in turn, is a consequence of the molecular environment of the hydrogen atom, a particular moiety can be identified by the shielding effect it has on the nucleus. From $\omega = \gamma B$ we see that the resonance frequency of all nuclei varies proportionally with the field strength. The difference relative to a standard sample is called the chemical shift and is measured in unitless numbers, given as ppm (parts per million, 10^6). Comparing all proton-containing chemical substances, the total range of ^1H nuclei resonance frequencies covers about 12 ppm. For instance, in an external magnetic field of 9.4 tesla, i.e., at a resonance frequency of about 400 MHz, the maximum difference in frequencies observed is only about 4800 Hz. To distinguish subtle differences between the molecules, the resolution of a good spectrometer must be much better, often values of 10^{10} (i.e., 0.4 Hz in our example) can be reached.

The macroscopic regime is the one that is directly accessible by the magnet designer. By introducing, on purpose, an inhomogeneity to the magnetic field by means of additional coils, B and therefore ω are made functions of the position. Of course, this only makes sense if each value of the field B occurs only once in the entire sample volume, so that an unambiguous assignment of the position is possible. The most obvious solution is the generation of a linear field dependence $B(\mathbf{r}) = B_0 + \mathbf{gr}$ for which inversion of the frequency into position is directly applicable. The following chapter will address this relationship.

What we have said up to now can be summarized in a simplified graphic representation of a basic NMR pulse sequence. The effects of either the microscopic or the macroscopic regime on the magnetization are visualized by the schematic picture given in Figure 2, which

relates the behavior of the magnetization (the broad arrows in the sketches at bottom) with the events that take place in the transmitter/receiver unit of the spectrometer (top row). At the beginning, the longitudinal magnetization is in equilibrium and no signal is detected. The first rf pulse (it is called a 90° pulse as the pulse duration is just long enough to rotate the longitudinal magnetization by that angle) delivers **M** to the transverse plane and creates transverse magnetization. Here, the x in the subscript of 90° indicates a rotation about the x axis to place the transverse magnetization along the y direction. Immediately after such a 90° pulse it still possesses its original magnitude but is forced to precess in the transverse plane about $\mathbf{B}_0$, inducing a signal in the receiver coil, the so-called free induction decay (FID). The transverse magnetization (also called coherence) is a sum of many contributions, originating from different spin positions inside a molecule as well as from different regions in space. Both effects - which we earlier termed microscopic and macroscopic - and also some others, generate a certain spread of local fields B and of Larmor frequencies ω, so that the individual contributions to the initial (maximum) magnetization start to "fan out" - note that the plot in Figure 2 must be understood as the rotating frame, i.e., we assume a point of view that is rotating with the carrier frequency of the transmitting radio field about the z axis. Some partial magnetizations (they are also called isochromats) precess faster, others precess slower than the average. Eventually, their vectors add up to zero and no signal is detected in the receiver. The 180° pulse "flip" all isochromats around, so that the faster ones suddenly find themselves at the trailing edge, but because the physical reason for their precession frequency has not changed, they begin to catch up with the slower ones. This process goes completely unnoticed by the operator of the NMR spectrometer, because the isochromats remain in a decoherent state relative to each other, and their vectorial sum is still zero. Only after a time that is exactly twice the separation between the two rf pulses do they get in phase again, and in this moment, the broad arrow, the complete magnetization, is regained, but now in the direction opposite to where it had pointed to immediately after the first rf pulse. This is because the 180° rotation was performed about the x axis, as depicted in Figure 2. By changing the phase of the rf pulses, i.e., by changing the axis about which the rotation of the magnetization vector takes place as discussed above, the final direction of this arrow can be chosen at will. The recovered magnetization induces a voltage in the receiver coil, seemingly out of nowhere - this is the so-called spin echo that Erwin Hahn saw for the first time in 1950, much to his surprise (see his memo about the discovery of the echo at the beginning of this book). The second half of this echo is identical to the FID at the beginning of the sequence, apart from their initial signal amplitudes due to microscopic or macroscopic processes that have happened to the system during the time between the FID and echo acquisition. Comparing echo and FID amplitudes can give a first starting point for analyzing the dynamics that are taking place in the sample; using the echo and continuing the procedure with the application of more rf pulses allows one to recycle the very same magnetization many times and extract even more information from its behavior.

The microscopic and macroscopic field dependences are the two basic building blocks of NMR. The second one is essentially what this book is about, NMR Imaging. However, the first one - the basic principle of NMR spectroscopy - is always present, and can be exploited as additional information in an NMR image to distinguish different species in a heterogeneous sample, something that no other imaging technique is able to achieve with such large versatility and specificity.

One can probably guess that NMR is more complicated than this short description suggests. Just a few of the complications arising in a "real" experiment are: how to distinguish between the different influences (microscopic and macroscopic) on the resonance frequency; how to generate three-dimensional images from the simple linear dependence of the field strength; how to measure motion; and how to deal with the myriad of various microscopic effects arising from interactions of the nuclei with each other and with the external fields.

2 Fundamentals of NMR Imaging

In this section, we will describe three building blocks of NMR imaging: phase encoding, frequency encoding and slice selection. All three are related to the signal by the fourth equation:

$$\omega(\mathbf{r}) = \gamma|\mathbf{B}(\mathbf{r})| = \gamma(|\mathbf{B}_0| + \mathbf{gr}) \tag{6}$$

Here we have introduced the position dependence of the magnetic field through its first derivative, the gradient vector $\mathbf{g}$, which renders the resonance frequency proportional to the position of the spin, $\mathbf{r}$. More precisely, the gradient has the properties of a 3×3 tensor because the derivatives of all three orthogonal components of $\mathbf{B}$ need to be computed. However, $\mathbf{B}$ is usually taken as pointing in the z direction, and its x/y components are negligible just as their spatial derivatives are. Note that the product $\mathbf{g} \cdot \mathbf{r}$ indicates that only those components of the position vector which are parallel to the gradient direction possess a different resonance frequency.

We now have to face the question: how can we express the imaging experiment by a mathematical formalism? To begin with, a physical object can mathematically be described by a density function of position: $\rho(\mathbf{r})$. If we apply an rf pulse to this object, and record the signal from the sample following the influence of the gradient, it will consist of contributions from all volume elements of the sample. In order to generate the image of the object, we will have to modify the weighting function (the effective gradient g turned on during the time t, hence $\mathbf{g}t$) to reconstruct the actual spin-density distribution. This approach is equivalent to a scattering experiment which is known from many fields of materials research: a wave of defined properties (wavelength, polarization) is aimed at an object and the scattered waves are investigated in terms of the above mentioned weighting function, which corresponds to the reciprocal space. The principle is the same whether light, X-rays, phonons or particles such as electrons and neutrons are considered; for the last of these, it is their wave properties that define the scattering effect. For instance, the structure of a crystal is obtained from an X-ray or neutron scattering pattern, which is related to the Fourier transform of the density function of the scattering centers, averaged over the whole sample. The Fourier transformation translates information from the reciprocal space, or k-*space*, to the direct space, or r-*space*; $\mathbf{k}$ and $\mathbf{r}$ are therefore Fourier conjugate variables.

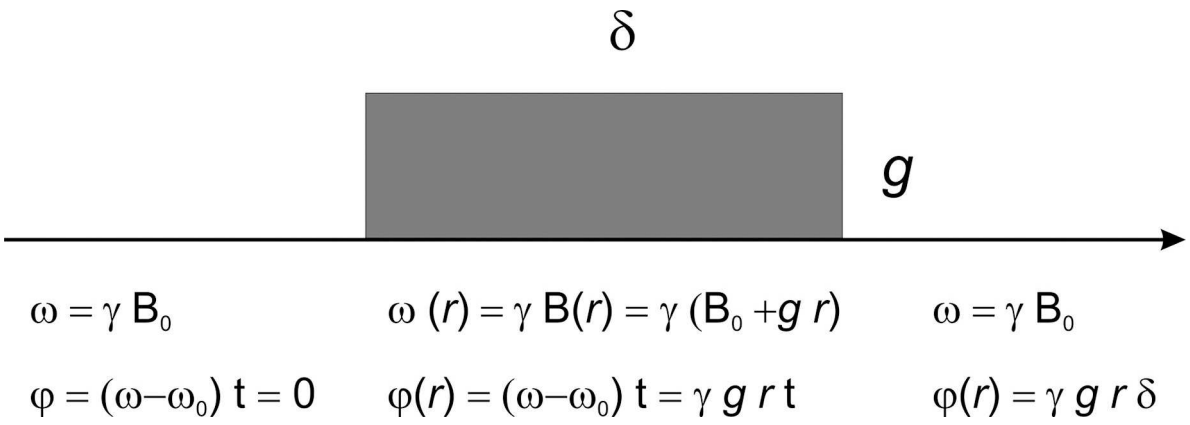

Figure 3: Effect of a pulsed magnetic field gradient of strength $\mathbf{g}$ on the phase of a signal contribution originating from spins at position $\mathbf{r}$. Prior to the gradient pulse, all spins experience the constant magnetic field B_0 and thus possess the same Larmor frequency; the phase shift relative to this average value is zero. During the gradient pulse, the field becomes position-dependent and a phase shift ϕ is accumulated that is proportional to position $\mathbf{r}$ and time t. After the gradient pulse (i.e., after completion of the phase encoding step), the spins memorize their individual phase shifts $\phi = \gamma\mathbf{gr}\delta$.

In a similar fashion, the information in NMR imaging is sampled in the reciprocal k-*space* and is then Fourier transformed into r-*space*, thereby reproducing the spin-density distribution $\rho(\mathbf{r})$, or *shape*, of the object. There is, however, one major difference that makes NMR a particularly strong tool for investigating matter: unlike the classical scattering techniques, which only provide an intensity measure as their result, the NMR information is a complex number and also contains the phase of the signal. By applying field gradient pulses, the position can be encoded into the phase of the signal as a function of $\mathbf{k}$, while its magnitude remains available for other information such as additional k-*space* dimensions, or chemical information via the modulation of the signal magnitude according to the gradient weighting function or the precession frequencies of the sample. This is the principle of multi-dimensional imaging, including imaging containing chemical shift resolution.

Let us now derive the equations that relate the spatial information to the signal behavior. As we have seen previously, a spin at position $\mathbf{r}$ possesses a Larmor frequency $\omega(\mathbf{r}) = \gamma|\mathbf{B}(\mathbf{r})| = \gamma(|\mathbf{B}_0| + \mathbf{gr})$. It is convenient to subtract the reference value, given by the "average" field, $\omega_0 = \gamma|\mathbf{B}_0|$, so that we obtain the frequency difference relative to an (arbitrarily chosen) position $\mathbf{r} = 0$:

$$\omega(\mathbf{r}) - \omega_0 = \gamma\mathbf{gr} \tag{7}$$

In NMR, data acquisition is demodulated with the carrier frequency corresponding to the magnetic field strength in use, ω_{rf}, which is chosen usually close to ω_0. Now assume that the gradient $\mathbf{g}$ is applied only during a certain interval δ. We call this a gradient pulse hence the frequently used term "pulsed field gradient (PFG) NMR" and it can be of arbitrary shape, but a rectangle with sharp edges is often used and facilitates the following discussion (see Figure 3). After the gradient pulse is switched off, the difference in frequencies leads to an accumulated phase shift, $\phi = [\omega(\mathbf{r}) - \omega_0]\delta$, with respect to the reference. Thus, the resulting phase shift of spins at position $\mathbf{r}$ following a gradient pulse of duration δ and strength $\mathbf{g}$ can be written as

$$\phi = \gamma\mathbf{gr}\delta \tag{8}$$

If we consider that the signal generated by the precessing magnetization is a complex number, the phase shift created by this gradient pulse leads to the NMR signal, which is the multiplication of the unperturbed NMR signal with the phase factor $exp[i\phi(\mathbf{r})]$. In order to compute the total signal arising from all spins within the sample with a spin-density distribution $\rho(\mathbf{r})$, we simply have to integrate all phase factors over the entire volume:

$$\begin{aligned} S(\mathbf{k}) &= \int \rho(\mathbf{r}) exp[i\phi(\mathbf{r})] d\mathbf{r} = \int \rho(\mathbf{r}) exp[i\gamma\mathbf{gr}\delta] d\mathbf{r} \\ &= \int \rho(\mathbf{r}) exp[i2\pi\mathbf{kr}] d\mathbf{r} \end{aligned} \tag{9}$$

In this equation, we have made the replacement $k = (1/2\pi)\gamma\mathbf{g}\delta$ in order to introduce the Fourier conjugate variable to $\mathbf{r}$. This is because formally Eq. (1.6) is a Fourier transformation. What we really want to know is the shape of the sample, $\rho(\mathbf{r})$, which we can derive by applying the inverse Fourier transformation to the signal function:

$$\rho(\mathbf{r}) = \int S(\mathbf{k}) exp[-i2\pi\mathbf{kr}] d\mathbf{k} \tag{10}$$

However, in order to be able to apply the inverse Fourier transformation, we need to know the dependence of the signal not only for a particular value of $\mathbf{k}$ (one gradient pulse), but as a continuous function. In practice, it is the Fast Fourier Transform (FFT) that is performed rather than the full, analytical Fourier Transform, so that the sampling of k-space at discrete, equidistant steps (typically 32, 64, 128) is being performed.

The recipe for the first building block of NMR imaging, the phase encoding, thus goes like this: apply a phase gradient of effective area $\mathbf{k}$; acquire the signal $S(\mathbf{k})$; repeat for a number of

different equidistant values of **k**; perform the inverse Fourier transformation to reconstruct the spin-density function of the sample, $\rho(\mathbf{r})$. The variation of gradients is symbolized by diagonal lines in Figure 4. Note that variation of the phase encoding gradient along one direction, say

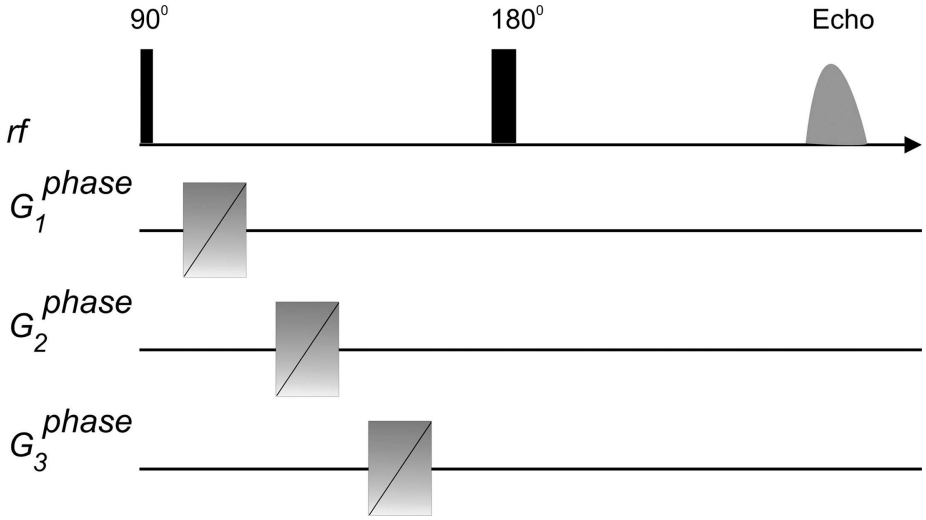

Figure 4: Phase encoding scheme in three dimensions. Three pulsed gradients in orthogonal directions are applied and are varied independently of each other (symbolized by the diagonal line). The actual timing of the gradients is arbitrary provided they are placed between the rf pulses and before the acquisition of the echo signal. In practice, the gradients are often applied simultaneously. The indices 1, 2 and 3 represent orthogonal directions with no priority being given to a particular choice of combinations.

k_x, allows the reconstruction of the profile only in this direction, $\rho(x)$. An example of this is shown in Figure 5, where the projection of a cylindrical object (such as a test tube filled with water) is depicted with the aid of simulated data. A series of FIDs is drawn in succession, a typical way of saving the data in a single, long vector file where each FID is being acquired in the presence of a particular gradient value, so that the range $-k_{x,max} \ldots k_{x,max}$ is covered and $k_x = 0$ is in the center, giving maximum signal intensity. Figure 5 also demonstrates the effect of an insufficient coverage of k-*space* on the image quality: if at the largest value of k_x used, the signal has not yet vanished, cut-off artifacts in the image do arise. However, extension of the sequence towards two- or three-dimensional encoding is straightforward, the only requirement being that all gradient pulses are stepped independently of each other. They might be applied either simultaneously or sequentially, they only have to be placed somewhere between the first excitation of the sample by an rf pulse and the final signal acquisition (see Figure 4). Equation (10) already contains this possibility; however, in Eq. (11) we have split the three orthogonal components and express the same relationship by a three-fold integral to highlight the three-dimensional nature of the experiment:

$$\rho(x,y,z) = \int S(k_x,k_y,k_y) exp[-i2\pi k_x x] exp[-i2\pi k_y y] exp[-i2\pi k_z z] dk_x dk_y dk_z \qquad (11)$$

The choice of gradient strength and duration can be optimized if the size of the object is known. From Eqs. (8 and 9) it becomes clear that a large gradient will lead to an ambiguous assignment of positions if the maximum phase angle exceeds 2π. One must therefore make sure that the difference between phase shifts generated for spins at the extreme ends of the sample is smaller than 2π for each different value of the gradient. In other words, $2\pi > 2(\gamma g_{max} \delta r_{max})/(n-1)$ if the gradient is varied in the range $-g_{max} \ldots + g_{max}$ in n steps. The coverage in r-*space* achieved with a particular set of gradient values is called the field of view (FOV) and is obtained from

$$FOV = \frac{n-1}{2} \frac{2\pi}{\gamma g_{max} \delta} \qquad (12)$$

For n gradient steps (n different k values), the image function $\rho(\mathbf{r})$ also possesses a resolution of n points as a consequence of the FFT procedure. Naturally, a larger g_{max} results in a better resolution if the number of steps n is chosen in such a way that the FOV slightly exceeds the object size itself. Note that a choice of a too small field of view will lead to so-called aliasing, i.e., those picture elements that correspond to a phase shift that exceeds the range π, will appear at the other side of the image so that superposition of two or more signal contributions into the image (backfolding) can occur. Figure 7 demonstrates the effect of backfolding for an FOV smaller than the object.

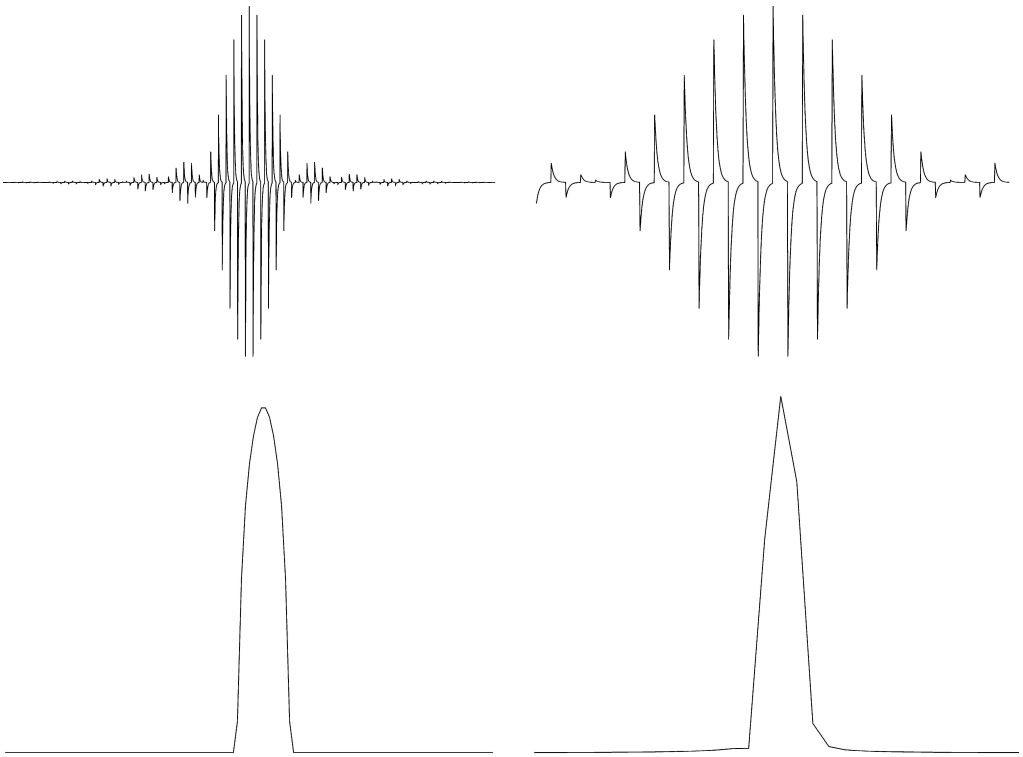

Figure 5: Simulated NMR data from a cylindrical object projected onto a direction perpendicular to the cylinder axis. Left: 128 steps of $k_x = 0$ were applied and the succession of FIDs are plotted; k-*space* is covered sufficiently well, i.e., the signal has decayed to zero at the largest values of $k_x = 0$. The Fourier transform of the series of FIDs (taken from the first points or from the integrals over each FID) is a satisfactory representation of the projection of the sample shape. Right: only the central 32 $k_x = 0$ values were acquired; the Fourier transform suffers from bad resolution, but also from a non-vanishing baseline due to the fact that the signal at the largest $k_x = 0$ values had not vanished.

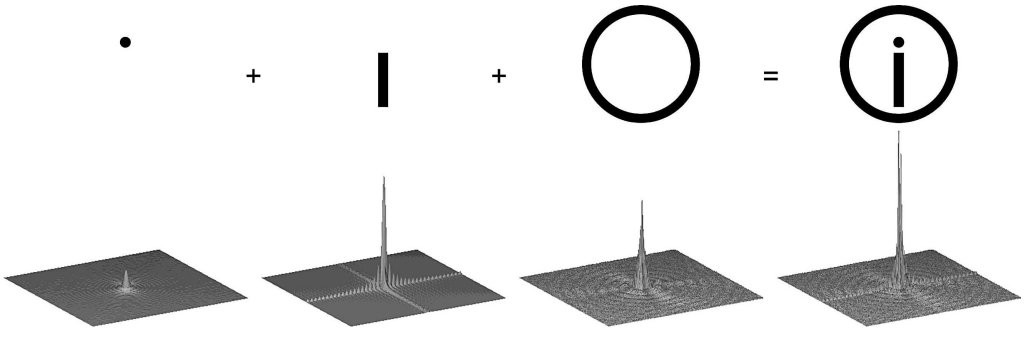

Figure 6: Left: the field of view has been chosen sufficiently large to cover the whole object; a correct image is obtained. Right: the field of view is only half as wide; the top and bottom portions of the object are folded back into the opposite side of the image. In a real NMR image, the assignment of position becomes ambiguous.

In order to demonstrate how the Fourier relationship works, Figure 6 shows what a two-dimensional object - a letter "i" in a circle - would look like in an NMR image, that is, its spin-density function $\rho(x, y)$ is shown, and the original signal function which is obtained by varying k, S(k_x , k_y). While S(k_x , k_y) is a complex function, only its real part is plotted. Because of the reciprocal relationship between $\mathbf{r}$ and $\mathbf{k}$, one can roughly say that the signal of high intensity in the vicinity of $\mathbf{k} = 0$ contains information about the general shape of the sample, and the small contributions at large $\mathbf{k}$ values is responsible for the fine structure, i.e., the resolution of the image. Although this is an oversimplified view, it is often helpful to keep this inverse relationship in mind and to estimate which effect the distortion of a particular

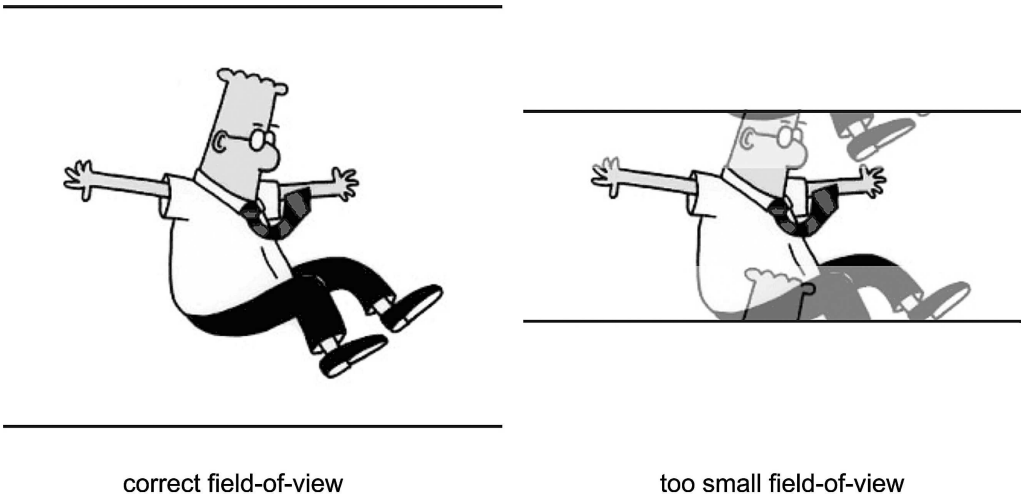

Figure 7: Two-dimensional objects in position space (top row) and their Fourier transform, corresponding to the shape of the signal function S(k_x , k_y) (bottom row). The actual object, a letter "i" inside a circle, is shown as the sum of three individual objects. Likewise, the Fourier transform is additive and the signal functions corresponding to each of the objects are shown for comparison.

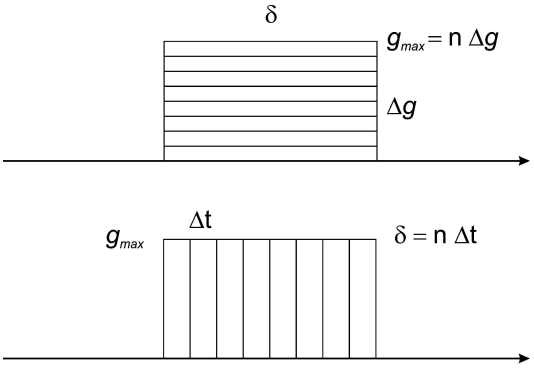

Figure 8: Demonstration of the formal equivalence of phase encoding and frequency encoding. In the top figure (phase encoding), the gradient of duration δ and strength g_{max} is split into eight equal steps of Δg. The signal is acquired n times (here n = 8), following a gradient of strength $i\Delta g$ where i is varied from 1 to n. In the bottom figure (frequency encoding), the gradient strength g_{max} is maintained but the total duration δ is split into eight equal steps, Δt. The signal is acquired n times (here n = 8), following a gradient of duration $i\Delta t$ where i is varied from 1 to n. In both cases, the signal corresponding to the same n = 8 k values between zero and $k_{max}$is sampled, where $k_{max} = (2\pi)^1 \gamma g_{max} \delta$.

part of the k-space data will have on the r-*space* image. In principle, only an analytical Fourier transformation of a continuous signal function $S(\mathbf{k})$ renders a perfect result; the compromise of a finite sampling of k-*space* gives rise to imperfections in the NMR image, which arise on top of potential physical problems, such as hardware imperfections. We will not discuss the

manifold possibilities of how image artifacts can arise and how they can be identified and compensated, but refer the reader to the textbooks at the end of this chapter, where this is discussed in great detail.

The foremost advantage of phase encoding is the fact that the signal is acquired in the presence of a homogeneous magnetic field; the signal thus contains the full spectroscopic information and this can be exploited to generate an image with individual spectra contained in each voxel representing the local chemical environment. This is one of the most powerful implications of NMR imaging. Just to name one important example, an inhomogeneous distribution of a mixture of liquids can be imaged while obtaining the full spectroscopic dimension, distinguishing the different phases and/or chemical species in the mixture. By this means, chemically selective, spatially resolved monitoring can be employed to study complex mixtures. The disadvantage of phase encoding is its inherent slowness. To generate a three-dimensional image with a satisfactory resolution of, say, $64 \times 64 \times 64$ points, an equivalent number of 64^3 individual signals have to be acquired. Allowing for a repetition time of 1 s between acquisitions, this corresponds to an experimental time of three days! The repetition time depends on the relaxation parameters of the sample; for liquids, it is in the order of several seconds so that three-dimensional phase-encoded images become prohibitively slow to measure.

One way out of this dilemma is the so-called frequency encoding technique. It is often referred to as an approach that is very different from phase encoding, but actually, it is only the timing of k-space sampling which is modified: in frequency encoding, the signal is acquired while the field gradient is present (see Figure 8); it is then referred to as a read gradient. Equation (8) is still valid, so that each subsequent point of acquisition at a given time t is under the effect of a longer read gradient field and thus contains a different phase angle. The full acquisition of one line in k-space takes only a few milliseconds; Fourier transformation of this signal, $S(\mathbf{k})$, again yields the profile of the object in the corresponding direction, $\rho(\mathbf{r})$, so that Eq. (10) also maintains its validity. In frequency encoding the time t is varied at constant gradient strength, thus it is also possible to write the signal of the frequency encoding technique as S(t), and its Fourier transformation directly renders the frequency distribution of spins in the sample. Because $\omega = \gamma \mathbf{gr}$, this frequency distribution is proportional to the spin-density distribution of the object. The difference in the phase encoding method is that the signal is acquired after it was subjected to a gradient field of duration δ and strength $\mathbf{g}$. Normally the gradient strength $\mathbf{g}$ is varied, and for each such step a new signal is utilized, formed either by excitation or echo formation.

While frequency encoding is time-saving because it samples one dimension in k-space in a single acquisition, its disadvantage is that the spectral information of the spin system is masked by the spatial encoding; the result will be a superposition of chemical shift and positional information. In other words, an object filled with a substance that has a spectrum consisting of two lines will render a double image because the physical reason for the frequency shift cannot be separated in a straightforward manner. However, substances with simple spectra such as water are often considered, or the separation between different spectral lines is negligibly small. This has turned a combination of frequency encoding in one dimension and phase encoding in one or two further dimensions into the most widespread imaging technique. Figure 1.9 gives a schematic example of a suitable pulse sequence, where the succession of gradients is arbitrary provided all phase encoding steps are completed before the beginning of the signal acquisition.

It must be mentioned that the reconstruction of a two- or even three-dimensional spin density distribution employing only frequency encoding is possible by varying the direction of the gradient, either by actual rotation of the sample or the gradient coil itself, or the rotation of the gradient fields by appropriate combinations of g_x and g_y gradients. The technique is known as backprojection/reconstruction and is similar to image processing routines used for generating 3D X-ray images in Computer Tomography (CT). While the advantage is that a

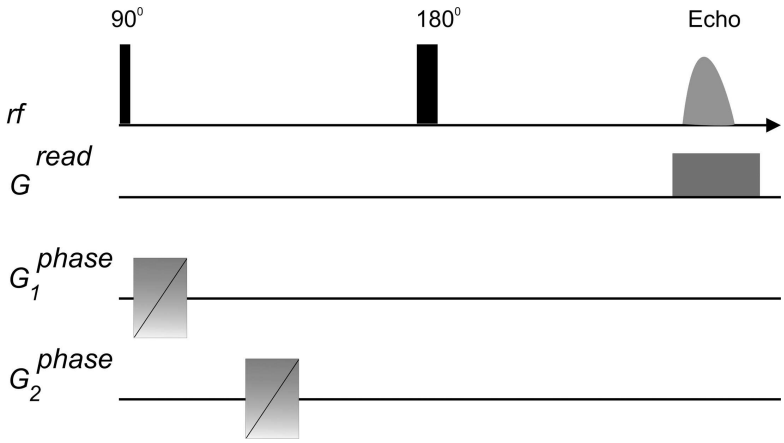

Figure 9: Schematic plot of a basic three-dimensional imaging pulse sequence with frequency encoding along one axis (read), and phase encoding along the two remaining orthogonal directions. The choice of directions is arbitrary, as is the position of the phase gradients within the sequence.

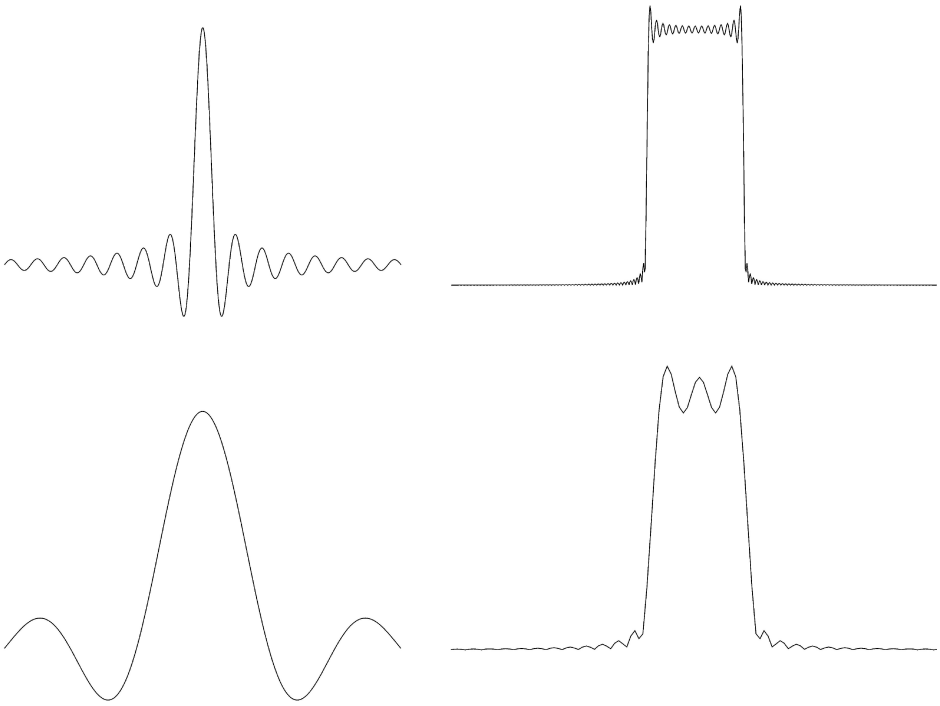

Figure 10: Soft rf pulses (left) in the shape of a sinc ($\sin x/x$) function, and their Fourier transforms (right), being equivalent to the excited slice in the presence of a constant magnetic field gradient. The well defined sinc function (top) produces an excitation that is a slice that deviates only slightly from a perfect rectangle. A cut-off sinc function, such as the one shown in the bottom part of the figure, produces a distorted slice profile which is, however, often sufficient for slice-selection in multidimensional imaging.

crude picture of the sample can be obtained immediately, long before the image acquisition is completed, some disadvantages are the lower signal-to-noise ratio, resolution and image quality, and that it does not allow the assignment of spectral features in the object. Because of its limited use for materials and process studies, we will not discuss the backprojection technique further.

Often, a cross-sectional image of an object contains all the necessary information that the researcher is interested in. However, such a two-dimensional cross section represents the integration over the third, non-encoded dimension. It is desirable to "cut out" a plane of the object, i.e., to produce an image of only a well defined slice without taking the remaining

volume into account. Slice selection is indeed possible; again, it exploits the fundamental relationship $\omega = \gamma B$, but in a slightly different sense. So far we have implicitly assumed that all rf pulses in the imaging sequences affect the whole number of spins in the same way. This is strictly true only for a hard pulse, i.e., a pulse with a bandwidth greatly exceeding the range of Larmor frequencies in the sample. The bandwidth of an rf pulse is given by the reciprocal of its duration: a short pulse possesses a broad frequency spectrum. More precisely speaking, the frequency spectrum of an rf excitation is the Fourier transform of its shape function. However, because of $\omega(\mathbf{r}) - \omega 0 = \gamma \mathbf{gr}$, the frequency is proportional to the position in the presence of a magnetic field gradient $\mathbf{g}$! We now only have to define the shape of the slice we want to excite, and perform the inverse Fourier transformation to find out what the equivalent pulse should look like. For a rectangular slice, this is particularly simple - the Fourier transform of a rectangle is the sinc function, $\sin x/x$ (see Figure 1.10). Generating an rf pulse of the correct length that is modulated by a sinc function will thus excite a rectangular slice of the sample and leave the remaining spins unaffected. Today pulses of virtually arbitrary shape can be generated with high temporal resolution. In practice, the function is cut at a certain number of periods to limit its duration, resulting in a somewhat imperfect shape of the slice, which is usually tolerated (see Figure 10). In typical imaging, the shaped pulse or soft pulse has a duration in the order of milliseconds, compared with the hard pulse of some tens of microseconds. The terms "hard" and "soft" can thus also be understood in the sense of the power level of the pulses, which necessarily is much higher if a very short pulse must achieve the same 90° rotation of the magnetization. The shape of any rf pulse can be chosen in such a

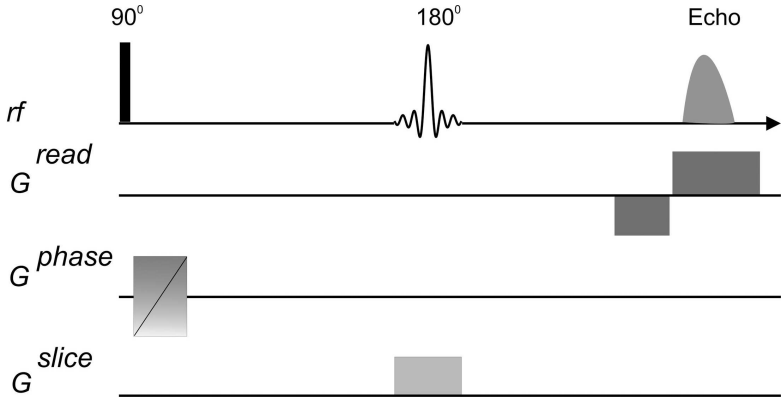

Figure 11: Typical basic three-dimensional imaging sequence with slice selection, frequency encoding and phase encoding in three orthogonal directions. The compensating lobe for the read gradient is drawn as a rectangle with negative intensity directly before the actual read gradient. The shape of the 180° rf pulse is drawn schematically to indicate that a soft pulse is used.

way that the excitation profile is a rectangular slice. In the light of experimental restrictions, which often require pulses as short as possible, the slice shape will never be perfect. For instance, the commonly used 90° pulse is still acceptable, while a 180° pulse produces a good profile only if it is used as a refocusing pulse. Sometimes pulses of even smaller flip angles are used which provide a better slice selection.

From the three building blocks, we can construct a typical NMR imaging sequence that is routinely employed for acquiring slices of an extended object (see Figure 11). It consists of a slice selection gradient in one direction, a frequency gradient in a second and a phase encoding gradient in the third direction. The directions are orthogonal to each other and their order is arbitrary, hence the usual labeling by "read, phase, slice" instead of "x, y, z".

A final but important comment has to be added to the discussion of the sequence in Figure 11. The read gradient is preceded by a negative lobe of half its area. The reason for this is that one wants to scan the whole k-space dimension with the read gradient. If we could switch on the gradient and begin acquisition immediately, the first acquired point would represent

$\mathbf{k} = 0$ and only positive values of $\mathbf{k}$ would be scanned. By applying a negative lobe before acquisition, the origin is moved towards a negative value before acquisition is begun; applying a lobe with half of the negative area of the read gradient means that the condition $\mathbf{k} = 0$ appears at the center of the acquisition window. The timing of the sequence is such that the echo generated by the rf pulses also appears in this instance. It is called spin echo and refocuses the effect of constant background gradients, and also the spreading in brought about by the properties of the sample spectrum (see also discussion of Figure 2). The combination of negative and positive lobes of g_{read} also produces an echo, the gradient echo. It appears at the point in time when $\mathbf{k} = 0$, or, in other words, when $\int g_{read} dt = 0$, i.e., the total effect of all gradients in the read direction vanishes. The integral is the mathematical definition of the area of the gradient, or the zeroth moment of the gradient,m_0. We will see in the following section why it makes sense to use this general nomenclature.

Part II
Application.

3 Study of aerogels.

3.1 Introduction to aerogels

Aerogel is a solid-state substance similar to gel where the liquid component is replaced with gas. The result is an extremely low density solid with several remarkable properties, most notably its effectiveness as an insulator. It is nicknamed frozen smoke, solid smoke or blue smoke due to its semi-transparent nature; however it feels like foam to the touch. Aerogel was first created by Steven Kistler in 1931, as a result of a bet with Charles Learned over who could replace the liquid inside a jam (jelly) jar with gas without causing shrinkage. The first results were silica gels. Aerogel can be made of many different materials; Kistler's work involved aerogels based on silica, alumina, chromia, and tin. Carbon aerogels were first developed in the early 1990s.

3.1.1 Properties.

Aerogels are composed of 90-99.8% air with typical densities of $3 - 150 mg/cm^3$. Aerogel feels like hard foam. Pressing softly does not leave any mark on the gel; pressing harder will leave a permanent dimple. Pressing hard enough will cause a catastrophic breakdown in the sparse structure causing it to shatter like glass (known as friability). Despite the fact that it is prone to shattering, it is very strong structurally, able to hold over 2000 times its own weight. Its impressive load bearing abilities are due to the dendritic microstructure, in which spherical particles of average size 2-5 nm fuse together into clusters. These clusters form a three-dimensional highly porous structure of almost fractal chains, with pores smaller than 100 nm. The average size and density of the pores can be controlled during manufacture. Aerogel is a remarkable thermal insulator because it almost nullifies three methods of heat transfer (convection, conduction or radiation). It is a good convective inhibitor because air cannot circulate throughout the lattice. Silica aerogel is a good conductive insulator because silica is a poor conductor of heat. (Metallic aerogel, on the other hand, is a better heat conductor.) Carbon aerogel is a good radiative insulator because carbon absorbs the infrared radiation that transfers heat. The most insulative aerogel is silica aerogel with carbon added to it. SEAgel is a material similar to organic aerogel, made of agar. Due to its hygroscopic nature, aerogel feels dry and acts as a strong desiccant. Since it is mostly air, it appears semi-transparent. The color it does have is due to Rayleigh scattering of the shorter wavelengths of visible light by the nanosized dendritic structure. This causes it to appear bluish against dark backgrounds and whitish against bright backgrounds. Aerogels by themselves are hydrophilic, but chemical treatment can make them hydrophobic. If moisture is absorbed, they will usually cause a structural change of contraction etc. and deteriorate; however, degradation can be prevented by turning them hydrophobic. The aerogel which has hydrophobicity to the interior can prevent degradation, even if a crack reaches deeper than its surface, compared with the aerogel that was turned hydrophobic only of their surface. Hydrophobic treatment makes processing easy because it allows the use of a water jet cutter.

3.1.2 Silica aerogel.

Silica aerogel is the most common type of aerogel and the most extensively studied and used. It is a silica-based substance, derived from silica gel. The world's lowest-density solid is a silica aerogel (the latest and lightest versions of this substance have a density $1.9 mg/cm^3$, 1/530

as dense as water), produced by the Lawrence Livermore National Laboratory. Silica aerogel strongly absorbs infrared radiation. It allows the construction of materials that let light into buildings but trap heat for solar heating. It has extremely low thermal conductivity (0.003 W/(moK), which gives it remarkable insulative properties. Its melting point is 1,200 C (2,192 F). Silica aerogel holds 15 entries in the Guinness Book of Records for material properties, including best insulator and lowest-density solid. Silica aerogel can protect the human hand from the heat of a blowtorch at point blank range.

3.1.3 Carbon aerogels.

Carbon aerogels are electrically conductive. They are composed of particles with sizes in the nanometer range, covalently bonded together. They have very high porosity (over 50%, with pore diameter under 100 nm) and surface areas ranging between 400-1000 m^2/g. They are often manufactured as composite paper - non-woven paper made of carbon fibers, impregnated with resorcinol-formaldehyde aerogel, and pyrolyzed. The composite aerogel paper is frequently used for electrodes in capacitors, or deionization electrodes. Due to their extremely high surface area (about 800 m^2/g), carbon aerogels are used to create supercapacitors, with values ranging up to thousands of farads. The capacitances achieved were 104 F/g and 77 F/cm^3. Carbon aerogels are also extremely black, reflecting only 0.3% of radiation between 250 nm and 14.3 μm, making them efficient for solar energy collectors. Carbon aerogels made of carbon nanotubes instead of graphite particles are highly elastic. They can be spun into fibers with strength greater than kevlar and unique electrical properties. Alumina Aerogels Alumina aerogels, especially metal-doped, are used as catalysts. Nickel-alumina aerogel is the most common combination. Alumina aerogels are also examined by NASA for capturing of hypervelocity particles; a formulation doped with gadolinium and terbium could fluoresce at the particle impact site, with amount of fluorescence dependent on impact velocity.

3.1.4 Uses.

The Stardust dust collector with aerogel blocks. (NASA) There are a variety of tasks for which aerogels are used. Commercially, aerogels have been used in granular form to add insulation to skylights. After several trips on the Vomit Comet, one research team has shown that producing aerogel in a weightless environment can produce particles with a more uniform size and reduce the Rayleigh scattering effect in silica aerogel, thus making the aerogel less blue and more transparent. Transparent silica aerogel would be very suitable as a thermal insulation material for windows, significantly limiting thermal losses of buildings. Its high surface area leads to many applications, such as a chemical absorber for cleaning up spills (see adsorption). This feature also gives it great potential as a catalyst or a catalyst carrier. Aerogel particles are also used as thickening agents in some paints and cosmetics. Aerogel performance may be augmented for a specific application by the addition of dopants, reinforcing structures, and hybridizing compounds. Using this approach, the breadth of applications for the material class may be greatly increased. Commercial manufacture of aerogel blankets began around the year 2000. This blanket is a composite of silica aerogel and fibrous reinforcement that turns the brittle aerogel into a durable, flexible material. The mechanical and thermal properties of the product may be varied based upon the choice of reinforcing fibers, the aerogel matrix, and opacification additives included in the composite. One manufacturer of this aerogel composite may be found in the link below. NASA used aerogel to trap space dust particles aboard the Stardust spacecraft. The particles vaporize on impact with solids and pass through gases, but can be trapped in aerogels. NASA also used aerogel for thermal insulation of the Mars Rover and space suits. Aerogels are also used in particle physics as radiators in Cherenkov effect detectors. ACC system of the Belle detector, used in the Belle Experiment at KEKB, is a recent example of such use. The suitability of aerogels is determined by their low index of

refraction, filling the gap between gases and liquids, and their transparency and solid state, making them easier to use than cryogenic liquids or compressed gases. Their low mass is also advantageous for space missions. Resorcinol-formaldehyde aerogels (polymers chemically similar to phenol formaldehyde resins) are mostly used as precursors for manufacture of carbon aerogels, or when an organic insulator with large surface is desired. They come as high-density material, with surface area about 600 m^2/g.Metal-aerogel nanocomposites can be prepared by impregnating the hydrogel with solution containing ions of the suitable noble or transition metals. The impregnated hydrogel is then irradiated with gamma rays, leading to precipitation of nanoparticles of the metal. Such composites can be used as eg. catalysts, sensors, electromagnetic shielding, and in waste disposal. A prospective use of platinum-on-carbon catalysts is in fuel cells.

3.1.5 Production.

Silica aerogel is made by drying a hydrogel composed of colloidal silica in an extreme environment. Specifically, the process starts with a liquid alcohol like ethanol which is mixed with a silicon alkoxide precursor to form a silicon dioxide sol gel (silica gel). Then, through a process called supercritical drying, the alcohol is removed from the gel. This is typically done by exchanging the ethanol for liquid acetone, allowing a better miscibility gradient, and then onto liquid carbon dioxide and then bringing the carbon dioxide above its critical point. The end result removes all liquid from the gel and replaces it with gas, without allowing the gel structure to collapse or lose volume. Resorcinol-formaldehyde aerogel (RF aerogel) is made in a way similar to production of silica aerogel.Carbon aerogel is made from a resorcinol-formaldehyde aerogel by its pyrolysis in inert gas atmosphere, leaving a matrix of carbon. It is commercially available as solid shapes, powders, or composite paper.

4 Visualization of gas flow and diffusion in porous media (aerogels).

The transport of gases in porous materials is a crucial component of many important processes in science and technology. In the present work, we demonstrate how magnetic resonance microscopy with continuous flow laser-polarized noble gases makes it possible to "light up" and thereby visualize, with unprecedented sensitivity and resolution, the dynamics of gases in samples of silica aerogels and zeolite molecular sieve particles. The "polarizationweighted" images of gas transport in aerogel fragments are correlated to the diffusion coefficient of xenon obtained from NMR pulsed-field gradient experiments. The technique provides a unique means of studying the combined effects of flow and diffusion in systems with macroscopic dimensions and microscopic internal pore structure. Flow and diffusion through porous media represent a vast field of study with many scientific and engineering applications, including catalysis, water purification, soil mechanics, and petroleum engineering. A detailed understanding of the complexities of flow and diffusion in porous materials is essential for the design, development, and optimization of catalysis and adsorption. Often, the design of such processes must resort to trial and error, because experimental techniques such as particle image velocimetry and laser Doppler anemometry are limited when it comes to high-resolution studies of flow through opaque porous samples.NMR spectroscopy and imaging are commonly used for noninvasive measurements of flow and diffusion of liquids and plastomers. Their application to gases, however, has been hampered by poor signal to noise ratio, a consequence of the low-density medium. In this contribution, we demonstrate a method for visualization of gas diffusion and flow effects in porous solids via NMR microscopy, in which the signal sensitivity is enhanced by optical pumping of noble gases, providing a 10,000- to 100,000-fold increase of spin polarization over the natural thermal Boltzmann distribution. Such gas phase imaging in combination with

optical pumping has been gaining widespread interest in the context of medical research and clinical applications primarily for images of the respiratory system. Elegant work from the Duke University Medical Center, for example, has shown striking images of laser-polarized 3He and ^{129}Xe inside lungs with a variety of features, ranging from fully filled lungs to gas dynamics in pulmonary airways. The present visualization technique for porous media is based on the unique imaging contrast that laser-polarized gases provide under conditions of steady-state continuous flow. Because the imaging contrast derives from the transport of laser-polarized gases via flow and diffusion, direct "snapshots" of gas flow and diffusion in the porous samples can be obtained. Interaction of nonreactive xenon gas with the surface of a host material leads to a distortion of its large electron cloud reflected by the wide chemical shift range of around 300 ppm. Therefore, it is possible to image xenon gas selectively in different environments based on its chemical shift position. This highly useful feature is not available with other gases. Microporous and mesoporous materials such as zeolites (pore diameter $< 10\mathring{A}$) and aerogels (pore diameter $< 500\mathring{A}$) are used to illustrate the potential of the technique. Aerogels are ultralight porous materials, typically based on silica, with densities ranging from 0.003 to 0.25 g/cm^3. The aerogel chemical composition, microstructure, and physical properties can be controlled at the nanometer scale, giving rise to unique optical, thermal, acoustic, mechanical, and electrical properties. NMR spectra of laser-polarized xenon gas flowing through fragments of silica aerogel at two different partial pressures are depicted in Fig. 12A. Xenon occluded within the aerogel gives rise to a signal with a chemical shift separated by about 25 ppm from that of pure (bulk) gas phase. The solid line corresponds to a gas pressure of 1 atm (0.5 atm of Xe and 0.5 atm of N_2), and the dashed line corresponds to a gas pressure of 4 atm (3 atm of Xe and 1 atm of N_2). Addition of nitrogen gas facilitates the optical pumping, although pure xenon gas can also be used with somewhat reduced signal intensity. The decrease in chemical shift with the higher pressure of gas occluded in aerogel fragments is in agreement with previous NMR data for xenon at thermal equilibrium. To produce "chemical shift selective" images, low power Gaussian-shaped 90 rf pulses are used (pulse width = 400 μs). Thus, images of xenon diffusing through aerogel fragments (Fig. 12B) can be separated from those of the bulk phase xenon gas (Fig. 12C). The gas diffusion around and into the material can be visualized by spin density images encoded with varying time delays between excitation pulses. NMR experiments normally involve a time delay between scans during which the longitudinal magnetization is restored to thermal equilibrium by spin-lattice relaxation. In the present methodology, which uses "externally prepared" magnetization, the 90 rf excitation pulse essentially destroys the magnetization created by optical pumping, and the system thus relaxes back to thermal equilibrium, yielding negligible imaging contrast for the gas phase. In this mode of imaging, therefore, the spin-lattice relaxation is effectively replaced by the transport of fresh laser-polarized ^{129}Xe via flow and diffusion. Fig. 2 shows the penetration of xenon into aerogel fragments as a function of the "transport time" (the time delay between excitation pulses) and the total gas pressure. NMR images of a higher pressure gas mixture (total pressure = 4 atm) penetrating aerogel fragments via diffusion are shown in Fig. 13 A-C, and a lower pressure gas mixture (total pressure = 1 atm) is shown in Fig. 13 D-F. For short time delays between the pulses, the images show xenon signal at the outer regions of the aerogel fragments (Fig. 13 A and D). The extent of xenon penetration into the material depends on the diffusion coefficient and can be estimated by the mean displacement $\bar{R} = (2Dt)^{1/2}$, where D is the diffusion constant and t is the time duration of the diffusion. The diffusion coefficient of xenon inside the aerogel fragments depends on the overall gas pressure; thus, it is possible to visualize different degrees of gas penetration into the material in a given time period by comparing experiments at different gas pressures. Diffusion coefficients of xenon gas at two pressures inside the aerogel fragments, D_{aero}, and in the bulk gas phase, D_{bulk}, are determined by pulsed-field gradient NMR experiments. For a lower pressure mixture (0.5 atm of Xe and 0.5 atm of N_2) we find $D_{aero}, = 0.65mm^2/s$, whereas the high pressure mixture (3 atm of Xe and 1 atm of N_2) yields $D_{aero} = 0.35mm^2/s$. Bulk phase xenon diffusion coefficients,

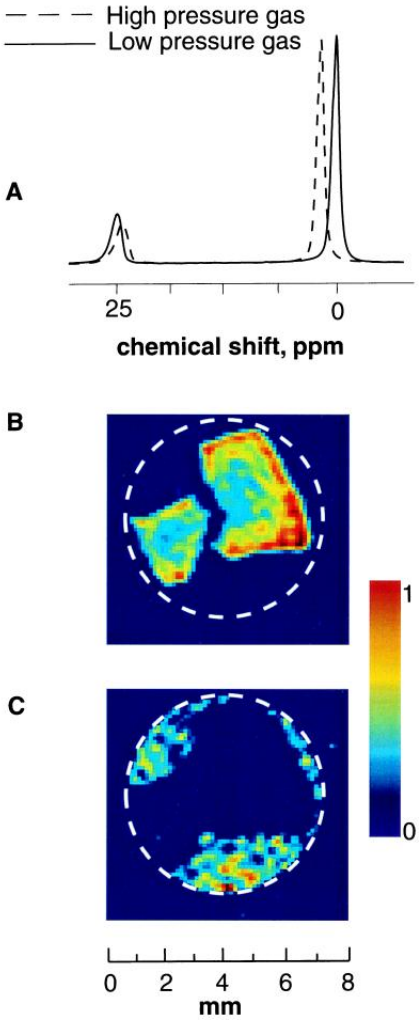

Figure 12: (A) NMR spectra of laser-polarized $X^{129}e$ flowing through aerogel fragments at two different pressures (T = 290 K). Xenon occluded in aerogel gives rise to a signal around 25 ppm, where the pure gas phase (bulk phase) at 1 atmosphere (atm; 1 atm = 101.3 kPa) has been used as a reference at 0 ppm. The solid line shows the spectrum recorded at 1 atm total pressure (0.5 atm of Xe and 0.5 atm of N_2), and the dashed line shows the result at 4 atm (3 atm of Xe and 1 atm of N_2). (B) Polarization-weighted images of laser-polarized xenon diffusing into aerogel fragments, based on chemical shift selection of the transition at 25 ppm (spectrum in A, solid line). The 2D magnetic resonance image slices (perpendicular to the flow) from the full 3D data set, with a resolution of $250 \times 250 \times 100\mu m$, are recorded at T = 290 K by using lower pressure gas mixture with a pulse time delay of 0.4 s. The white circle designates the wall of the sample container. (C) Polarization-weighted images of bulk laser-polarized xenon gas outside the aerogel fragments, based on chemical shift selection of the transition at 0 ppm (see Fig. 1A, solid line). The image is a 2D slice from the full 3D data set with a resolution of $250 \times 250 \times 100\mu m$, taken perpendicular to the flow with a pulse time delay of 0.4 s.

D_{bulk}, for low and high pressure mixtures are determined to be $5.5mm^2/s$ and $2.6mm^2/s$, respectively. The different degrees of gas penetration (e.g., Fig. 13, compare B and E) can be observed only for short time delays. For longer times, the material becomes saturated with polarized gas as seen in the images of Fig. 13 C and F. An interesting feature of the xenon images is the asymmetrical distribution of xenon spin density in the aerogel fragments at short time delays (indicated by the white arrows in Fig. 13 A and B), a consequence of the differential flow and accessibility of gas to the fragments. Fig. 12C shows that, for some regions, the gas flow is obstructed, and therefore at short time delays, the delivery of freshly polarized xenon is limited. Such circumstances arise, for example, for fragments close to the glass walls of the sample container and for areas of close contact between fragments.

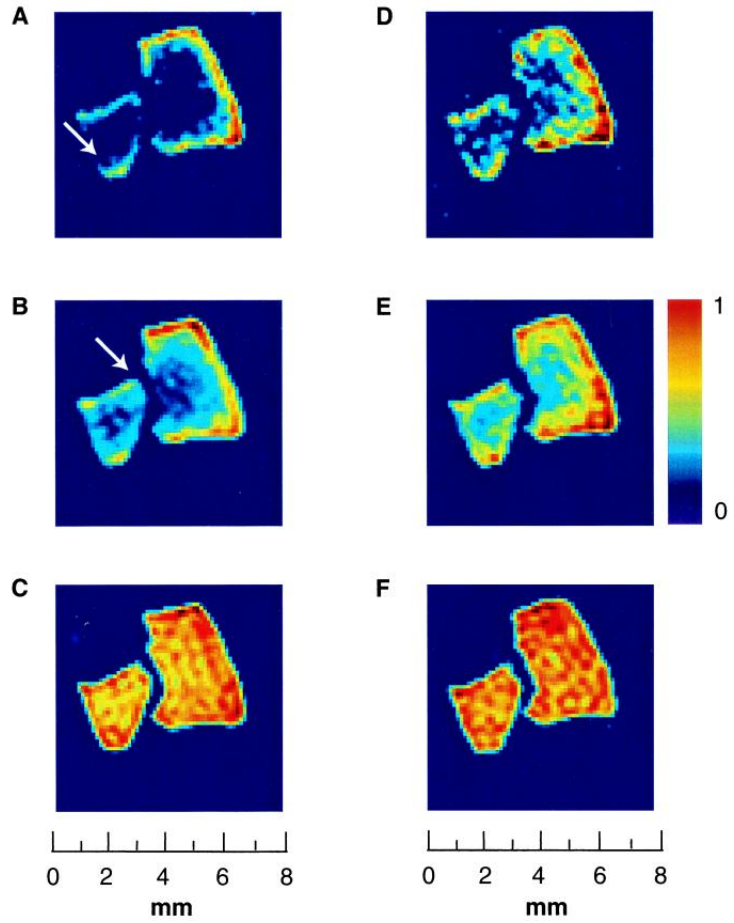

Figure 13: Penetration of laser-polarized xenon into silica aerogel fragments at two different pressures as a function of time delay between excitation pulses. Shown are 2D magnetic resonance image slices perpendicular to the flow from a 3D data set, with a slice thickness of 100 μm and an in-plane resolution of $250 \times 250 \mu m$. (AC) Magnetic resonance images of xenon adsorbed in aerogel fragments at high pressure (3 atm of Xe and 1 atm of N_2; spectrum shown in Fig. 1A, dashed line around 25 ppm). The diffusion coefficient of xenon at T = 290 K under these conditions is $D_{aero} = 0.35 mm^2/s$. The pulse delay times are 0.2 s (A), 0.4 s (B), and 2 s (C). (D-F) Magnetic resonance images of xenon adsorbed in aerogel fragments at lower pressure (0.5 atm of Xe and 0.5 atm of N_2; spectrum shown in Fig. 1A, solid line at 25 ppm). The diffusion coefficient of xenon at T = 290 K under these conditions is $D_{aero} = 0.65 mm^2/s$. The pulse delay times are 0.2 s (D), 0.4 s (E), and 2 s (F). The asymmetrical distribution of xenon spin density inside the aerogel fragments, for the shorter time delays, reflects the close proximity of fragments to each other and to the walls of the container, which attenuates the efficient accessibility of polarized gas to the fragments (white arrow).

As shown in Fig. 14, particle contact and restricted gas flow also affect the images of gas penetration into zeolite particles. The technique thus presents a useful means of mapping out the dynamics of gases flowing over a bed with porous fragments, a common situation in industrial processes that use heterogeneous catalysts. The xenon atom has a diameter of about 4.4 $\AA$, making it an appropriate probe of 13 $\times$ zeolites with estimated pore size of about 7-8 $\AA$. The NMR spectrum of laser-polarized xenon flowing through 13X zeolite particles of diameter $\cong$ 2 mm shows two signals: one from bulk phase ^{129}Xe (reference peak) and a second one at 130 ppm arising from xenon occluded within the zeolite. A 2D magnetic resonance image slice of the occluded xenon, taken from the full 3D data set, in a plane parallel to the flow is shown in Fig. 3B, whereas Fig. 14C depicts a slice through one particle, perpendicular to the flow. The most apparent feature of Fig. 14 B and C is the high intensity in the outer area of the particles with signal rapidly decaying toward the center. The penetration of xenon into the material is indeed dominated by diffusion, but spin-lattice relaxation reduces

the signal before the particles can become saturated with polarized gas, in contrast to the situation for the aerogel fragments. Polarization-weighted xenon NMR imaging with variable time delays can be used to map out gas phase dynamics between particles with a resolution of $100 \times 100 \times 100 \mu m^3$, a compelling advance in gas phase imaging. The method described in this contribution uses a unique imaging contrast modality, based on the transport of laser-polarized gases via flow and diffusion, providing snapshots of the gas dynamics, thereby allowing the visualization and investigation of transport phenomena in porous materials. By using the continuous-flow apparatus, polarization-weighted images can also be used as complementary data to the quantitatively direct, albeit time-consuming, NMR measurements of flow profiles and diffusion coefficients.

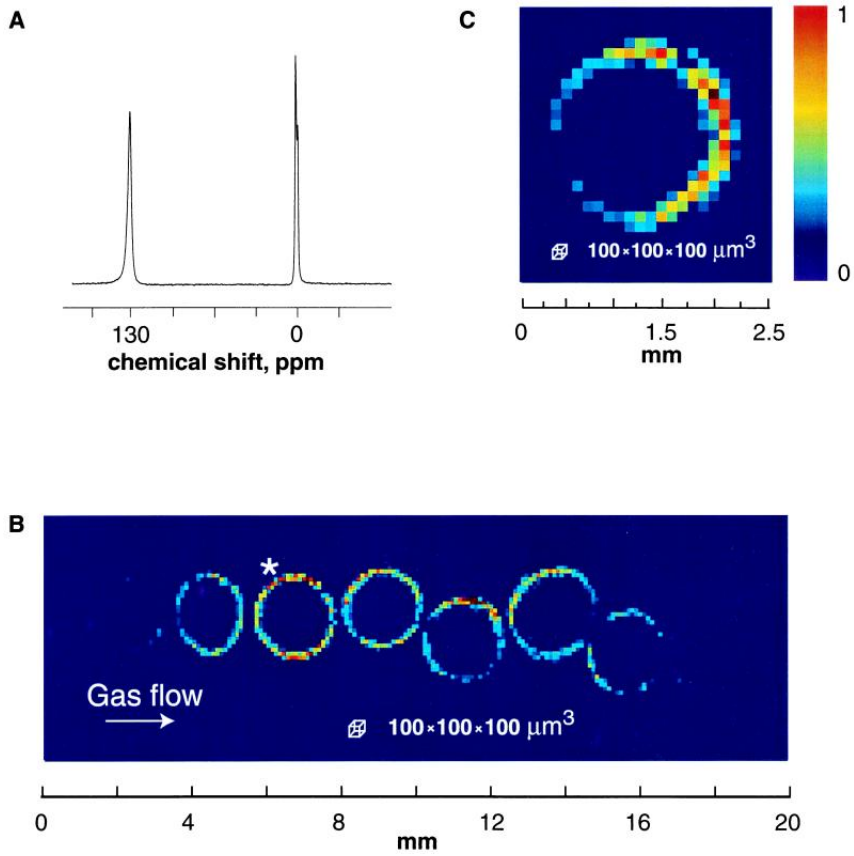

Figure 14: (A) NMR spectrum of laser-polarized xenon flowing through spherical particles of 13 × zeolites (T = 290 K). Xenon occluded within the zeolite gives rise to a signal at 130 ppm, referenced to bulk phase xenon gas at 0 ppm (1 atm of Xe and 1 atm of N_2). (B) Magnetic resonance 2D image: longitudinal slice (along the direction of flow) from a full 3D data set for xenon occluded in zeolite particles. The 3D data with a resolution of 100 μm in all three dimensions ($64 \times 64 \times 256$ points) are Fourier-transformed with no zero-filling or smoothing filters. Spin-lattice relaxation reduces the polarization of xenon before the pellet is saturated completely with laser-polarized ^{129}Xe. The asymmetric intensity of spin density in the pellets reflects close contact of neighboring particles, which interferes with the efficient flow and accessibility of polarized gas to the particles. (C) Magnetic resonance 2D image: transverse slice (perpendicular to the direction of flow) from a full 3D data set as described for B. The asterisk in B indicates which particle is depicted in the slice. The low signal intensity on the left-hand side of the particle is caused by its close proximity to the glass walls of the container, which interferes with the flow accessibility of polarized gas.

5 Applications of One-sided Access NMR.

5.1 Water content measurement.

In a moist material, the hydrogen density is directly proportional to the overall water content within the detected object volume. NMR is a well established method for fast and accurate moisture determination in pharmaceutical, cosmetic and foodstuff industry. Successful aquametric applications have also been reported in technical materials as concrete, wood and polymers . The diagram in Fig. 4 shows a typical calibration curve, representing the functional dependence between the amplitude A of the ^1H-NMR signal and the water content in light-weight concrete, expressed in mass-percent. The correlation is almost proportional. Such a calibration curve can be applied for almost all mineral construction materials (except materials with high ferromagnetic particle content). Depending on the measuring time, the inaccuracy of determined water content is typically between 0.3 and 1 mass-%. Moisture values as low as 0.5% can still be detected. Even if the material contains other hydrogenous substances besides water, it is still possible to accurately determine the moisture content.

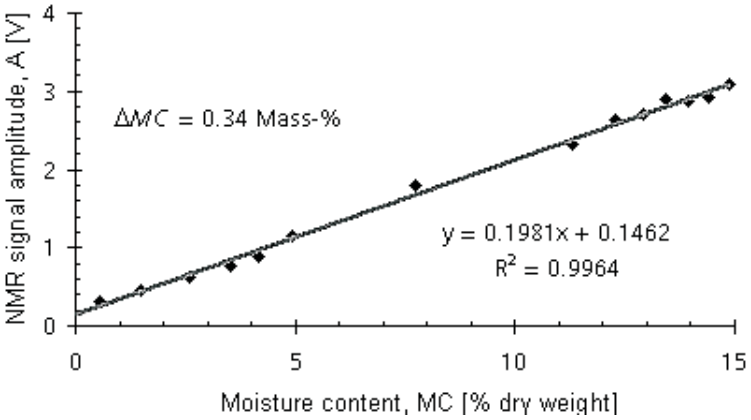

Figure 15: Water content measurement in light-weight concrete with NMR; calibration to gravimetric (destructively) determined moisture content.

5.1.1 On-site detection of water depth-profiles in concrete pillars.

In Fig. 15 application and results of a moisture profile measurement on a lightweight concrete pillar are presented. The red line in the diagram shows the moisture profile as it was determined on-site. The profile could be determined up to the maximum measuring depth of the used OSA NMR device, which was 26 mm. The entire measurement with a resolved depth-increment of 1 mm and an inaccuracy better than 0.5 % has taken approximately 30 minutes.

This result indicates a water content increasing strongly in depth. The strength of this result was not clear, because the reinforcing steel bars embedded in concrete could eventually result in false readings of the water content. In order to verify the measurement result, a drilling core 150 mm in length was drawn leaving out the steel reinforcement bars Later this drilling core was investigated in the laboratory. For the purpose of measuring the moisture distribution across the entire length of this sample, it was cut into 3 pieces of about 50 mm in length. By measuring from the upside as well as from the bottom side of each piece, it was possible to determine the moisture content at each point of the drilling core despite the limited maximum measuring depth of 26 mm. This "laboratory" moisture profile is shown as black line in the diagram of Fig. 15. Apart from small differences at the beginning, probably as a result of the one-day delay between on-site measurement and sampling, a good accordance between

the "on-site" profile and the "laboratory" profile is obvious. Therefore it can be concluded that in the present case the steel reinforcement does not have a significant influence on the NMR measurement. Note, that the strongly decreased moisture contents at about 50 and 100 mm are a consequence of the cutting process. Finally, the integral moisture contents of the cut pieces have been determined by gravimetry (weighing, drying and re-weighing). The moisture contents determined by this method are shown as grey straight line in the diagram. With OSA NMR current moisture situation and variations of water distribution during wetting and drying can be observed directly on the building component. Entire building constructions can be inspected in a complete non-destructive manner, without the need for impairing its integrity or its appearance by taking a sample. By determining the water tightness of building structures, environmental durability problems can be detected in an early stage, preventing unexpected fatal damage due to moisture ingress. A further application is to monitor the drying process in fresh concrete or cement floorings.

5.2 Determination of density and moisture depth-profiles in wood panels.

The profiles of moisture and density across the panel thickness are the most important measuring parameters for characterizing and controlling the product quality in fabrication of chip (and fiber) wood panels. Usually, the density profile of small samples is determined by laboratory methods. Nowadays, the raw density profile in wood panels can be measured on-line with devices based on Compton backscattering. But due to the similar scattering and absorption properties of solid wood and moisture, these methods do not accurately determine the dry wood density, which is by for more interesting than the raw density. Based on the analysis of

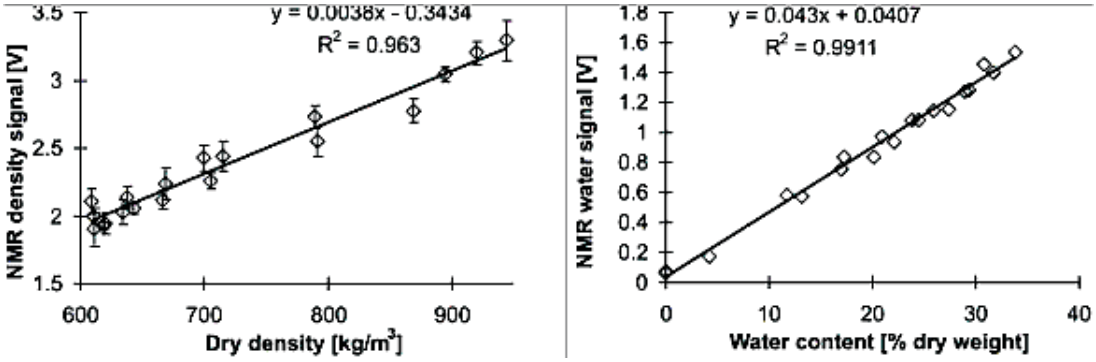

Figure 16: Simultaneous density and moisture determination in wood panels; by analyzing the T_2 relaxation curve the signal contribution from hydrogen in solid wood (left diagram) can be separated from the signal contribution of moisture (right diagram).

the T_2 relaxation curve, solid and liquid wood components can be quantitatively distinguished by NMR. Here the relaxation curve is composed of 2 overlapping exponential curves representing hydrogen in solid wood and hydrogen in wood moisture. By analyzing the measuring curve the relative hydrogen content of both components can be determined. On this approach wood moisture as well as the dry wood density can be measured in a single procedure (see Fig. 16). By using OSA NMR, profiles of moisture and density can be determined on-line during panel fabrication.

5.3 Monitoring of early-age concrete hardening.

Fresh concrete develops in strength over time. Initially, after casting, the concrete is supported within a formwork until it gains sufficient strength to support its own weight. Early

age damage as well as increased susceptibility to detrimental influences from the environment (reduced durability) can often be traced to insufficient strength development prior to loading of the structure. Event though a variety of methods to measure the properties of fresh concrete are already available, monitoring the strength development in early-age concrete is still an unsolved testing problem. Conventional methods, as for example the Vicat needle test, the slump test, the flow table test, etc. are not objective because the results are highly dependent on the measuring device and the measuring procedure. None of these methods allows continuous monitoring of material properties from the fresh to the hardened state, because they are destructive. During hydration a part of the mixing water is chemically combined in hydration products and the residual water is confined in pores, which gradually decrease in size as cement hydration proceeds. These processes strongly affect the T_1 and T_2 relaxation times. On the other side, the same changes of cement-stone's microstructure affecting the relaxation times are also responsible for the development of the physical properties, as strength and tightness. Therefore, measures of T_1 (T_2) allow for monitoring the strength development in hardening concrete. By use of OSA NMR instrumentation this method is a new approach in order to continuously monitor the hardening of concrete on a building component. The hardening behavior of five different concrete mixtures as well as pure cement pastes has been investigated in the present study. The specimens were prepared by using conventional Portland cement. Different water-to-cement ratios (w/c) as well as enrichment of some specimen with a retarder (Tetra-Potassium-Pyrophosphate) should provide a wide range of hardening behavior. The concrete hardening was monitored over three days. Starting with the preparation, the T_2 relaxation curve measuring of each specimen was measured after hardening times t_h of approximately 1, 2, 3, 4, 5, 6, 8, 9, 23, 25, 27, 29, 31, 59 and 60 hours. The left diagram of Fig. 17 shows

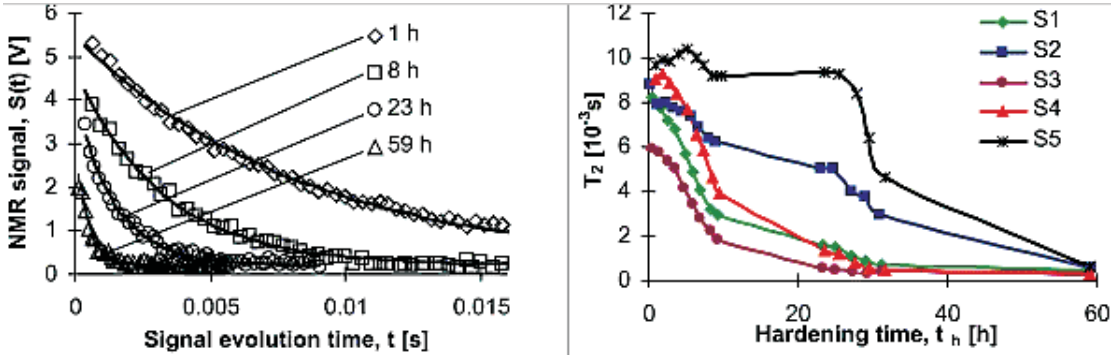

Figure 17: Monitoring of concrete hardening by T_2 relaxation curve measurements. As hardening proceeds the decay of the T_2 relaxation is getting faster (left diagram), which is equivalent to the decrease of the relaxation time T_2 as a function of hardening time(right diagram).

the evolution of the T_2 relaxation curve of a specimen for 4 different hardening times. It is much of evidence that the decay is accelerating as hardening, i.e. cement hydration proceeds. Fitting the experimental data to an one-exponential approximation function provides the time constant of the decay curves, which is the relaxation time T_2. From the beginning up to the end of hardening, this relaxation time shows typically a strong decrease (right diagram of Fig. 17). In case of cement paste or concrete without retarder (S1, S3 and S4 in the right diagram of Fig. 17), this decrease is moderate in the first 2-3 hours after mixing water and cement. This "Induction Period" is followed by an accelerated decrease ("Acceleration Period") up to 20-30 hours and finally hydration and with it T_2 decrease are slowing down ("Decay Period"). Hence the T_2 evolution follows the hydration progress and with it the qualitative behavior of strength development in concrete. The influence of a water-to-cement ratio (w/c) which is only 0.4 instead of 0.6 can be observed by comparing the hydration behavior of specimen S1 and S3. Specimens with retarder (S2 and S5) show the most peculiar behavior. As expected, the "Acceleration Period" is strongly delayed. The strong dependence between T_2 (and also

T_1) and the hardening state in cementitious materials is a well-known fact. In literature it was shown, that this correlation can be used to predict the strength-development in early-age concrete . The concern of the present study was to demonstrate the feasibility of monitoring the hardening in concrete by conducting T2 measurements not only with laboratory NMR equipment but also with OSA NMR, offering the possibility to inspect early-age concrete on a building side.

5.4 Determination porosity and pore-size distribution in soils.

So-called NMR logging tools are used for on-site characterization of subsoil earth formations in regards to porosity, oil / water saturation, pore-size distribution and permeability. These tools are used for the exploration of oil or water wells and the determination of building ground stability. Architecture and mode operation of logging NMR are very similar to OSA NMR. Based on the experiences from NMR-INSPECT development, a NMR logging tool for borehole exploration is constructed at IZFP at the moment. Simultaneously to this hardware development, experimental NMR methods are studied, which are capable to determine microstructure dependent properties of rock materials, as porosity, pore-size distribution and water permeability. Fig. 18 shows the measuring results of the T_1 relaxation time distribution in soils of unconsolidated material. Two specimens with different grain distributions have been investigated. The blue curves in the foreground of the diagrams show the NMR T_1 distributions, which correspond to the pore-size distributions. The beams in the background show the grain distributions derived from sieve analysis. It is obvious, that there is good qualitative agreement between NMR measuring data and sieve analysis.

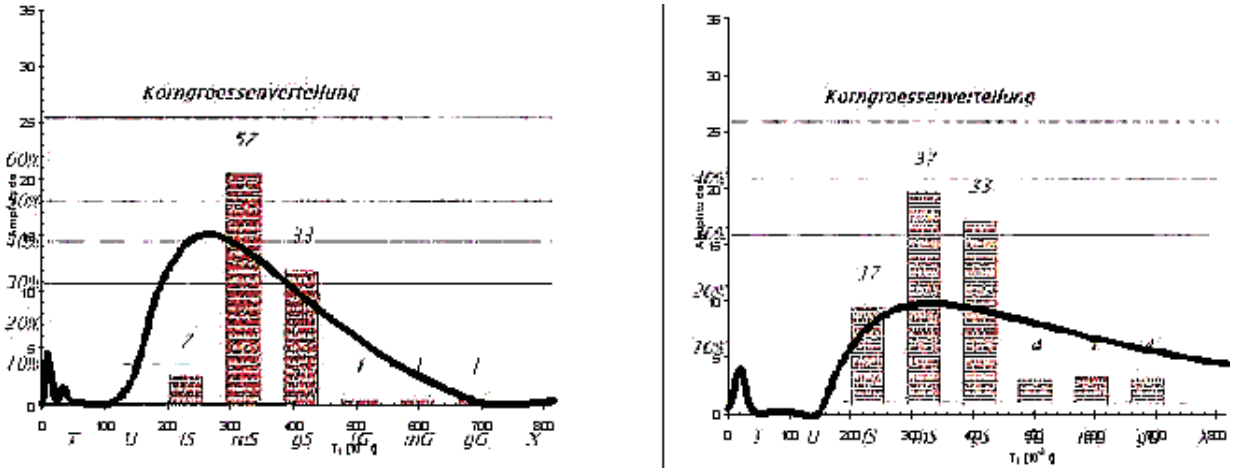

Figure 18: Grain-size and pore-size distribution in unconsolidated material (soil); brown bars: grain-size distribution, determined by sieve analysis; blue lines: T_1 relaxation time distribution (NMR measurement), corresponding to pore-size distribution; left: fine grain distribution (without gravel); right: coarse grain distribution (with gravel).

5.5 Other cases.

5.5.1 Restricted Diffusion.

Diffusion in pores is quite different than in bulk. Water molecules near pore walls cannot freely move. Therefore they spend more time in one position when they are in proximity of walls than when they are in the center of pores. This can be well seen by diffusion weighted NMR experiment. A notch (2.6 mm wide) drilled in a plastic glass was filled with water and imaged in by 1D diffusion weighted imaging sequence. When gradients for diffusion weighting were low (b) the 1D profile well followed the shape of the notch (a). As the gradients were increased

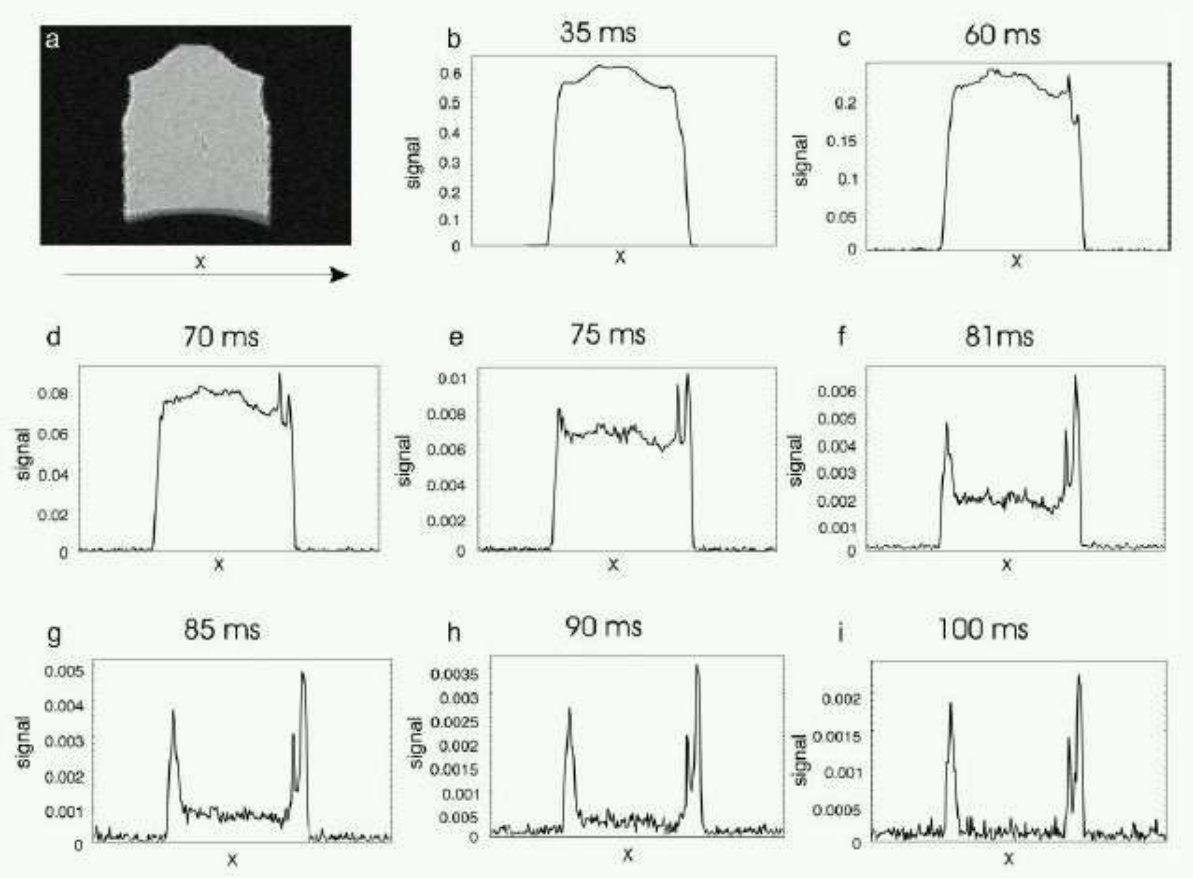

the signal from the central region of the notch became significantly more attenuated than the signal of water molecules in the proximity of notch walls (e-g). This came to the extreme (h-i) when practically no signal was obtained from the center of the notch and still enough signal from the region next to walls. This was due to restricted motion of water molecules at notch walls.

5.5.2 Water migration in porous materials.

Water in pores of many materials is often unwanted since it may reduce their durability and lifetime. From that perspective it is important to understand how water migrates into these materials. Water migration can be accurately monitored via high-resolution magnetic resonance imaging in non-magnetic and non-conductive materials. We were particularly interested in situations where at the beginning of migration the material was completely dry and at the end was saturated with water. Water migration was monitored by 1D profiles of water concentration along the direction of migration. For the experiment, cylindrically-shaped samples

Figure 19: Experiment.

of dental cement with a diameter of 3 mm and a length of 5 mm were used. The long surface of the samples was coated with a varnish to prevent water migration into the cement, while the ends of the samples were left uncoated. One end of the cylinder was exposed to a constant water concentration, and the other end was in contact with the air around the sample. Images above depict water concentration (image intensity in color coded scale) as a function

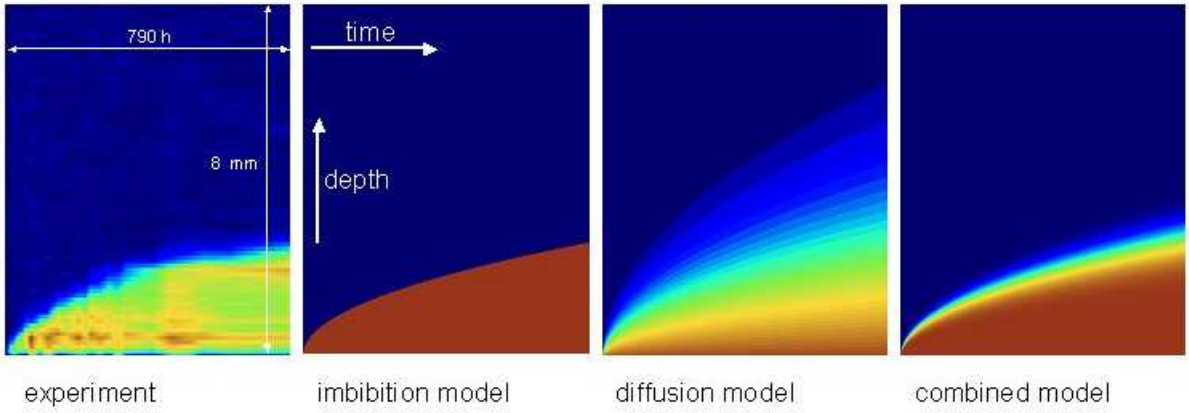

Figure 20: Results.

of depth (vertical axis) and time (horizontal axis) as measured in the experiment on dental cement. The experimental results were analysed by three different mathematical models: an imbibition model, a diffusion model, and a combination of both models. From the results it can be clearly seen that depth of the region saturated with water increases as the square root function of time.

5.5.3 Imaging fibers in an air spring.

One application of imaging in rubber product analysis is to determine the position of fibbers inside air spring bellows used in modern car suspension systems. Figure shows a car equipped with these air springs, a schematic drawing showing two crossed fiber layers to improve the resistance of the rubber balloon, and the measured images centered in each of the two layers. The fibers can clearly be observed.